JGR Solid Earth

Key Points:
- Granular mechanics modeling of fault gouge comprising velocity-weakening and velocity-strengthening components yields composite response
- A thin layer of talc (three particles) along the shear zone reduces shear strength, increases slip stability, and suppresses permeability gain
- Talc preferentially localizes in the shear zone, even for uniform mixtures, with this effect enhanced for preimposed layered structure

Correspondence to:
C. Wang,
cuw179@psu.edu

Ensemble Shear Strength, Stability, and Permeability of Mixed Mineralogy Fault Gouge Recovered From 3D Granular Models

Chaoyi Wang[1] ID, Derek Elsworth[1,2] ID, and Yi Fang[1,3] ID

[1]Department of Energy and Mineral Engineering, EMS Energy Institute, and G3 Center, The Pennsylvania State University, University Park, PA, USA, [2]Department of Geosciences, The Pennsylvania State University, University Park, PA, USA, [3]Institute for Geophysics, Jackson School of Geosciences, The University of Texas at Austin, Austin, TX, USA

Abstract We conduct numerical shear experiments on mixtures of quartz and talc gouge using a three-dimensional (3D) distinct element model. A modified slip-weakening constitutive law is applied at contacts. We perform velocity-stepping experiments on both uniform and layered mixtures of quartz and talc analogs. We separately vary the proportion of talc in the uniform mixtures and talc layer thickness in the layered mixtures. Shear displacements are cycled through velocities of 1 and 10 μm/s. We follow the resulting evolution of ensemble shear strength, slip stability, and permeability of the gouge mixture and explore the mesoscopic mechanisms. Simulation results show that talc has a strong weakening effect on shear strength —a thin shear-parallel layer of talc (three particles wide) can induce significant weakening. However, the model offsets laboratory-derived strong weakening effects of talc observed in uniform mixtures, implying the governing mechanisms may be the shear localization effect of talc, which is enhanced by its natural platy shape or preimposed layered structure. Ensemble stability $(a - b)$ can be enhanced by increasing talc content in uniform talc-quartz mixtures. Reactivation-induced permeability increase is amplified with increased quartz content before the maturation of shear localization. Postmaturation permeability enhances on velocity upsteps and diminishes on velocity downsteps. Talc enhances compaction at velocity downsteps, potentially reducing fault permeability. Evolution trends of stability relating to the composition and structure of the fault gouge are straightforwardly obtained from the 3D simulation. Local friction evolution indicates that talc preferentially organizes and localizes in the shear zone, dominating the shear strength and frictional stability of faults.

1. Introduction

Seismic events commonly occur on mature faults consisting of fault cores and damage zones (Faulkner et al., 2010). Frictional response and stability of faults are usually governed by fault gouge present in the fault core. Extensive studies have documented the friction and stability of fault gouge under varied stress conditions, shear velocity regimes, and fluid saturations in the laboratory using natural and synthetic samples (Fang et al., 2018; Ikari et al., 2011; Mair & Marone, 1999; Samuelson et al., 2009). Fault gouge can contain mixtures of frictionally strong tectosilicates and weak phyllosilicates (Collettini & Holdsworth, 2004; Faulkner et al., 2003; Vrolijk & Van Der Pluijm, 1999; Wintsch et al., 1995), including talc (Giorgetti et al., 2015; Moore & Lockner, 2011; Niemeijer et al., 2010a). Talc can be derived from the metamorphic alteration of ultramafic rocks with silica-saturated hydrothermal fluids and from dissolution of dolomite under the alteration of silica-rich fluids (D'Orazio et al., 2004; Escartín et al., 2008; Grasemann & Tschegg, 2012; Moore & Rymer, 2007; Peacock, 1987; Taylor & Huchon, 2002; Viti & Collettini, 2009).

Laboratory studies suggest that talc may exert a significant effect on the shear strength and slip stability of gouge mixtures. Gouge may be weakened by a > 50 wt % of talc if uniformly distributed (Moore & Lockner, 2011) but only ~4 wt % of talc is required to weaken the gouge in layered mixtures (Niemeijer et al., 2010). Laboratory shear tests using uniform mixtures of talc and calcite show that talc has a dominant effect on shear strength at weight percentages of ~20% or higher (Giorgetti et al., 2015). The study of layered gouge mixtures with talc, for example, layered talc sandwiched by frictionally strong minerals, has always been a challenge in the laboratory due to the difficulty in preparing a uniform and consistent talc layer, tracking localized shear deformation, and mechanistcally analyzing shear deformation within the gouge layer

during shearing. An alternative way to study the dynamic responses of gouge materials is to take advantage of numerical methods. One effective method is to conduct a similar study on friction evolution of synthetic fault gouge during dynamic shearing by distinct element methods (DEMs, Cundall & Strack, 1979). DEM has been successfully applied to the simulation of fault gouge and many other laboratory experiments on rocks and granular materials (Gao et al., 2018; Guo & Morgan, 2004; Morgan, 2004; Morgan & Boettcher, 1999; Sun et al., 2016; van den Ende et al., 2018; Wang et al., 2017). Granular gouge materials are represented by an assembly of particles that can move independently within preset degrees of freedom. The dynamics of particles are updated by explicit representation of Newton's second law, and the interaction of particles is evaluated by various constitutive contact models depending on different applications and scenarios.

DEM simulations of granular materials are usually carried out in two dimensions for equivalent media and with compensation mechanisms to represent suppressed out-of-plane displacements (Morgan, 1999; Morgan & Boettcher, 1999; Wang et al., 2017). Gouge models constructed in 2D are widely adopted due to the significantly lower computational cost. However, the shape and dimensionality of particles can also affect the maximum shear strength of simulated faults (Abe et al., 2011; Ferdowsi et al., 2014; Knuth & Marone, 2007). Additionally, 2D models typically fail to reproduce out of plane particle interactions, lack particle interlocking mechanisms, and exaggerate shear dilation. Studies have been conducted both numerically and experimentally to investigate the effects of particle dimensionality on the shear strength of faults (Knuth & Marone, 2007). Unusual fluctuations in shear strength evolution are observed in laboratory double direct shear experiments using metal rods (representing 2D particles). Unrealistically low shear strength is also observed, and this is believed to be caused by free rolling of the particles (rods).

The shear stability of faults is commonly described by rate and state friction law (Dieterich, 1992; Marone, 1998; Ruina, 1983). Shear stability of granular shear is analyzed by direct measurement of shear stress and shear displacement in the laboratory; it is also implemented in DEM simulations by introducing contact-based constitutive laws. A contact-based slip-weakening law has been implemented in 2D DEM simulations for slip stability analysis (Wang et al., 2017). Although a large number of studies and discussions have been carried out to investigate shear strength and slip stability of granular shear using 2D or 3D configurations (Anthony & Marone, 2005; Ferdowsi et al., 2014; Hazzard & Mair, 2003; Knuth & Marone, 2007), few studies have combined slip stability and permeability evolution of gouge mixture containing frictionally weak minerals using 3D DEM simulation.

In this study, we complete 3D DEM simulations of granular gouge in shear experiments using quartz and talc analogs. Specifically, we explore the shear strength, slip stability, and permeability evolution of the mixture in the configurations of uniform and layered mixtures (e.g., layered talc). The weight percentage of talc in these two configurations is systematically varied. By performing direct shear simulations with velocity steps, transitional behavior in shear strength and changes in the stability parameter $(a - b)$ are captured and its impact on permeability inferred. We present mechanistic analyses of this transitional behavior.

2. Method

A three-dimensional (3D) direct shear model is constructed for this study using the 3D particle flow code (Itasca Consulting Group. Inc.). We define a contact model and iteratively solve Newton's second law to interpret the dynamics of particle interaction. A slip-weakening law is incorporated for individual particle-particle contacts. In this study, quartz and talc analogs are tested on both uniform mixtures and layered mixtures.

2.1. Model Configuration

The 3D DEM model represents one symmetric half of the double direct shear configuration (Marone, 1998, Figure 1). In this model, gouge analogs are confined between two saw-tooth grooved platens consisting of particle clumps. The length of the shear platen is 20 mm. The thickness of the gouge sample assembly is approximately 5 mm including the platens; the exact thickness varies with mineral content. Virtual walls are generated outside of the assembly to prevent the extrusion of particles during shear. These virtual walls do not obey Newton's second law due to the lack of mass. However, they preserve linear elastic contact properties and can thus perform as elastic boundaries to the assembly.
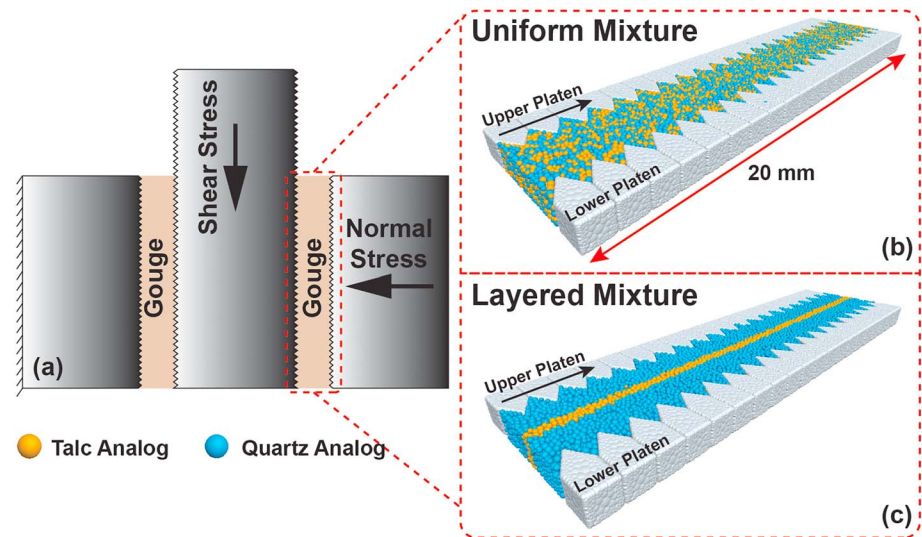
Figure 1. Model configuration represents one half of the double direct shear configuration (Mair & Marone, 1999). (a) Double direct shear configuration; (b) DEM model for homogeneous mixtures (red line marks the model scale; black arrow marks the direction of shear); (c) layered mixture. DEM = distinct element method.

The direct shear simulations are conducted under a normal stress (applied perpendicular to the shear direction) of 10 MPa with the stress magnitude maintained via a servo-loading algorithm. The algorithm constantly adjusts the relative velocity of the upper and lower platens to retain the normal stress within 0.5% of the preset magnitude (10 MPa in this study). The 3D model simulates the full process of direct shear by the following steps:

1. generate a domain, virtual walls, and shear platens;
2. generate loosely distributed mineral analogs with an initial target porosity of 55%, allowing initial particle overlaps;
3. equilibrate the assembly by iterating until the ratio of unbalanced forces to the sum of body force, applied force, and contact forces on one particle in all degrees of freedom (mechanical ratio) is less than 0.001;
4. activate the servo-displacement algorithm to compact the sample until the normal stress (10 MPa) is reached while maintaining the mechanical ratio below 0.001; and
5. actuate the upper platen in shear to a preset velocity and cycle between velocity steps.

The analog mixture is sheared through a full displacement of 500 at 1 µm/s with the velocity then up-stepped to 10 µm/s over a further 500 µm of shear displacement. The velocity is then decreased to 1 µm/s and the process repreated. The maximum shear displacement for each simulation is 3,500 µm, enabling a total of six successive steady states to be reached. The numerical simulation monitors the evolution of ensemble friction coefficient, sample layer thickness, average coordination number, and porosity of the gouge sample during dynamic shear. Shear stress is calculated from the unbalanced force on upper shear platen divided by effective shear area. Friction coefficient is then interpreted by the ratio of shear stress to normal stress. The sample layer thickness is calculated from the average distance between the two shear platens prescribing the outer boundary (the distance from the outer flat surface of the upper platen to the lower platen). Porosity is monitored in seven spherical control volumes distributed in the gouge along the shear direction. The diameter of each spherical control volume is 750 µm. The locations are ±4, ±3, ±2, and 0 mm offset the geometric center of the compacted sample before shear.

2.2. Contact Model

In order to reduce the rolling tendency of the uniformly spherical particles in the model and to thereby reproduce realistic particle interlocking effects, we use a contact model accommodating rolling resistance and linear elastic contact (Ai et al., 2011; Iwashita & Oda, 1998; Jiang et al., 2015; Wensrich & Katterfeld, 2012). This is effective in reducing the undesirable strong rolling effect of particles during simulation. Specifically, the contact model consists of linear elastic components in both the normal and shear
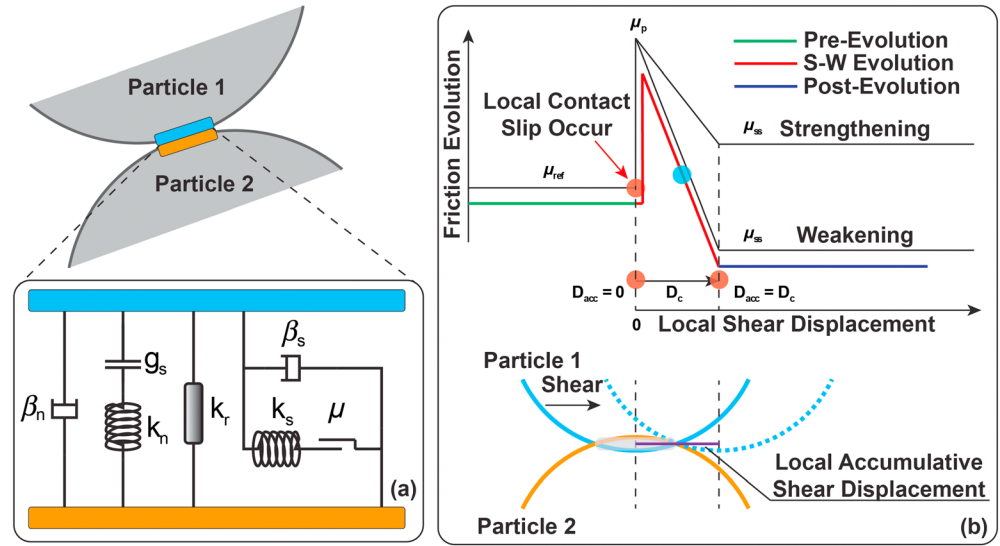
Figure 2. (a) Contact model between two particles comprises linear elastic components in the local shear and normal directions with a moment-based rolling resistant component (k_r); (b) modified slip-weakening constitutive relation acting at each particle-particle contact.

direction (Figure 2a). All components act at a vanishingly small contacting area, with only forces and moments transmitted. The contact force ($\boldsymbol{F}_c$) is resolved into normal (F_n) and shear components ($\boldsymbol{F}_S$). Magnitudes of shear force $\boldsymbol{F}_s$ are compared to a threshold F_s^μ, and if more than this magnitude allows contact slip with the friction coefficient evolving according to a slip-weakening constitutive relation. The iterative constitutive relation for normal and shear elastic components are

$$\boldsymbol{F}_c = -F_n\widehat{\boldsymbol{n}}_c + \boldsymbol{F}_S + \boldsymbol{F}_d \tag{1}$$

$$F_n = (F_n)_0 + k_n\Delta\delta_n \tag{2}$$

$$\boldsymbol{F}_s = (\boldsymbol{F}_s)_0 - k_s\Delta\boldsymbol{\delta}_s \tag{3}$$

$$F_s^\mu = -\mu_0 F_n \text{ (before slip initiates)}; F_s^\mu = -\mu F_n \text{ (after slip initiates)} \tag{4}$$

in which $(F_n)_0$, $(\boldsymbol{F}_s)_0$, and $\boldsymbol{F}_d$ are the normal force, shear force vector, and damping force vector (damping ratio of 0.2 is implemented in both normal and shear direction); $\widehat{\boldsymbol{n}}_c$ is the contact normal; k_n and k_s are the normal and shear contact stiffnesses; $\Delta\delta_n$ and $\Delta\boldsymbol{\delta}_s$ are the increments of local displacement and displacement vector in the normal and shear directions; μ_0 is the Coulomb friction coefficient of the contact before slip initiates (also μ_{ref}); and μ is the transient friction coefficient of the contact after slip initiates.

The contact moment ($\boldsymbol{M}_c$) is determined by the rolling resistance moment ($\boldsymbol{M}^r$) determined by rolling resistance stiffness k_r and local bend-rotation increment ($\Delta\theta_b$). $\boldsymbol{M}^r$ is updated as

$$\boldsymbol{M}^r = (\boldsymbol{M}^r)_0 - k_r\Delta\theta_b \tag{5}$$

$$k_r = k_s\overline{R}^2 \tag{6}$$

$$\frac{1}{\overline{R}} = \frac{1}{R^{(1)}} + \frac{1}{R^{(2)}} \tag{7}$$

in which $(\boldsymbol{M}^r)_0$ is the rolling resistance moment vector of the previous time step; and $\overline{R}$ is the contact effective radius calculated from the radii ($R^{(1)}$ and $R^{(2)}$) of two contacting particles.

The magnitude of rolling resistance moment is capped by a rolling resistance coefficient μ_r, particle properties (size, contact stiffness), and normal force. The magnitudes of rolling resistance moment ($\boldsymbol{M}^r$) is checked against a threshold limit (M^*), with M^* calculated according to equation (8). The rolling resistance moment

is set as M^* if the resultant rolling resistance moment is greater than the threshold. This mechanism works in a sense similar as Coulomb's law of friction as

$$M^* = \mu_r \overline{R} F_n \tag{8}$$

The implementation of this rolling resistance makes it feasible to simulate particle interlocking by restricting the rolling tendency of spherical particles.

When slip occurs, instead of evaluating frictional behavior using Coulomb's law of friction, a rate-and-state approach (Dieterich, 1979; Marone et al., 1990; Ruina, 1983; Scholz, 1998) is commonly applied. The rate and state friction laws are interpreted with a single degree of freedom elastic coupling system, and the associated constitutive relations implemented as

$$\mu(V, \theta) = \mu_0 + a \ln\left(\frac{V}{V_0}\right) + b \ln\left(\frac{V_0 \theta}{D_c}\right) \tag{9}$$

$$\frac{d\mu}{dt} = k\left(V_{lp} - V\right) \tag{10}$$

in which μ_0 is the reference friction coefficient prior to friction evolution; a and b are the empirical stability parameters associated with the material; V, V_{lp}, and V_0 are the current, load point, and reference sliding velocity, respectively; θ is the state variable; D_c is the characteristic slip distance; and k is the system stiffness.

The commonly accepted evolutions for the state variables are the Dieterich and Ruina laws as

$$\frac{d\theta}{dt} = 1 - \frac{V\theta}{D_c} \quad \text{(Dieterich law)} \tag{11}$$

$$\frac{d\theta}{dt} = \frac{V\theta}{D_c} \ln\left(\frac{V\theta}{D_c}\right) \quad \text{(Ruina law)} \tag{12}$$

Both laboratory and simulation studies show that rate and state friction laws adequately describe seismic and frictional healing during fault slip events. DEM simulations involve updating friction evolution at many active contacts in every time step. Implementation of full rate and state friction laws for all contacts is currently computational ineffective (Abe et al., 2002). To reduce the computational cost, we assume that the system stiffness is infinitely large and implemented a modified slip-weakening response at each contact. The slip-weakening law is described as

$$\mu_p = \mu_{ref} + a \ln\left(\frac{V_{lp}}{V_{ref}}\right) \tag{13}$$

$$\mu_{ss} = \mu_{ref} + (a - b) \ln\left(\frac{V_{lp}}{V_{ref}}\right) \tag{14}$$

$$\mu = \begin{cases} \mu_p & D_{acc} = 0 \\ \mu_p - \left(\frac{\mu_p - \mu_{ss}}{D_c}\right) D_{acc} & 0 < D_{acc} < D_c \\ \mu_{ss} & D_{acc} \geq D_c \end{cases} \tag{15}$$

in which μ_p is the peak friction coefficient at the initiation of evolution; μ_{ss} is the presumed steady state friction coefficient after evolution; μ_{ref} is the reference friction coefficient between particles; V_{lp} and V_{ref} are the load point velocity and reference velocity of the shear platens; a, b, and D_c are contact surface stability parameters and are not necessarily identical to the laboratory-derived values for rate and state friction; and D_{acc} is the accumulative shear displacement on the contact.

This constitutive relation is implemented for each contact of the assembly. The behavior of this modified slip-weakening constitutive relation is shown in Figure 2b. In the numerical implementation, the value of the current load point velocity and reference velocity is stored for each contact. The evolution of friction at contacts will evolve in the following manner:

Table 1

Model Parameters Including Calibrated Elastic Modulus for Quartz and Talc (Guan et al., 2012)

	Quartz analog	Talc analog	Unit
Density[a]	2650	2800	kg/m^3
Radius	25–50	25–50	μm
Interparticle friction	0.3	0.1	(−)
Effective modulus	35	1.0	GPa
Normal-to-shear stiffness ratio	1	1.5	(−)
Calibrated elastic modulus	9.35	0.94	GPa
Rolling resistance coefficient	0.5	0.3	(−)
Interparticle a value	0.0025	0.0050	(−)
Interparticle b value	0.0050	0.0025	(−)
Interparticle D_c	50	25	μm

[a]Density scaling (10^{12}) has been implemented in shear simulations; the corresponding time step is in the magnitude of 10^{-3} s. The influence of density scaling is discussed in section 5.2

1. The friction coefficient follows the (green) path shown in Figure 2b before local shear force reaches the friction threshold.
2. Once the local shear force reaches the threshold and triggers local slip, friction evolution follows the slip-weakening path (red path of Figure 2b).
3. The local friction coefficient reaches a steady state (purple path in Figure 2b). Note that the final steady state can be either velocity strengthening or weakening with both paths (black) shown for demonstration.

There are cases when a local slip on a contact halts before the full evolution of friction can occur. In such cases, the friction coefficient of the contact will remain as is (shown as the blue dot in Figure 2b). The evolution continues once the slip is reinitiated and when the contact is still active. If the contact is no longer active, due to large shear displacement, then the friction evolution will halt. When a new contact forms, the friction evolution always follows the three stages noted above.

2.3. Mineral Analogs

We use quartz and talc analog particles to represent analog mixtures. Quartz and talc exhibit importantly contrasting frictional properties. Quartz is frictionally strong but with velocity neutral or weakening, while talc is frictionally weak but with velocity strengthening (Ikari et al., 2011). It is observed both in nature and the laboratory that small amounts of talc can greatly weaken the shear strength of a mineral assembly comprising a majority of strong minerals in the matrix (Giorgetti et al., 2015; Moore & Lockner, 2011; Moore & Rymer, 2007).

The elastic modulus of granular materials is dependent on particle size distribution, particle shape, and mean stress and is usually much smaller than that of the intact bulk materials (Guan et al., 2012). In this model, the elastic interaction between particles is governed by a combination of local elastic stiffness in the normal and shear directions. The normal and shear stiffnesses are derived from a calibrated effective modulus (E^*) and normal-to-shear stiffness ratio (κ^*) via

$$k_n = \frac{AE^*}{L} \tag{16}$$

$$k_s = \frac{k_n}{\kappa^*} \tag{17}$$

where A is the virtual contact area between two particles, typically calculated with the smaller diameter of the two contact particles ($\pi R_{\min}^2$); L is the distance between the centers of gravity of the two particles.

Notably, the effective modulus (E^*) is not equivalent to the macroscopic elastic modulus. This is directly assigned as a contact property in a mesoscopic sense. Nevertheless, effective modulus is related to the macroscopic elastic modulus, and the normal-to-shear stiffness ratio is related to Poisson's ratio. Specifically, the effective modulus is calibrated through a series of pseudotriaxial compression simulation on packs of candidate quartz and talc analogs, respectively. The calibration process is defined as

1. make initial estimations of the effective modulus and normal-to-shear stiffness ratio;
2. generate an assemblage of candidate particles in a cylindrical vessel with a 3:2 height: diameter ratio;
3. conduct pseudotriaxial compression tests under a normal stress of 10 MPa up to an axial strain of 0.05%;
4. calculate the resultant macroscopic elastic modulus from the stress-strain relation; and
5. repeat by varying effective modulus and normal-to-shear stiffness ratios (#1) until the macroscopic estimate is within 3% of literature-derived values.

The calibrated contact properties are presented in Table 1.

In this study, there are often cases when contrasting mineral analog particles are in direct contact. In such cases, the contact surface stability parameters (a and b) are calculated from the harmonic average of parameters for the two contrasting materials. The normal and shear stiffnesses are connected in series. The

Table 2
Simulation Suite

Name	Quartz analog (wt %)	Talc analog (wt %)	Talc layer thickness[a]	Sample thickness[b] (μm)	Number of particles
qztc100-00	100%	0%	N/A	5998.91	19190
qztc90-10	90%	10%	N/A	5863.02	19117
qztc80-20	80%	20%	N/A	5762.72	19130
qztc70-30	70%	30%	N/A	5646.12	19076
qztc60-40	60%	40%	N/A	5519.43	19132
qztc50-50	50%	50%	N/A	5453.57	19121
qztc40–60	40%	60%	N/A	5393.31	19139
qztc30-70	30%	70%	N/A	5364.67	19197
qztc20-80	20%	80%	N/A	5347.15	19198
qztc00-100	00%	100%	N/A	5381.38	19192
qztc005	95.9%	4.1%	1 (~125 μm)	5958.33	19170
qztc010	91.9%	8.1%	3 (~250 μm)	5920.28	19114
qztc015	87.9%	12.1%	5 (~375 μm)	5908.96	19116
qztc020	83.4%	16.6%	8 (~500 μm)	5869.70	19063
qztc030	76.6%	23.4%	10 (~750 μm)	5810.17	19026

[a]The relative thickness of the talc analog layer is determined by the approximate number of particles across the initial talc layer with the approximate width in micron also listed. [b]The sample thickness is measured at the initiation of shear.

contact surface friction coefficient (μ) and the characteristic slip distance (D_c) are determined by the smaller value of the two particles.

3. Simulation

We study the evolution of shear strength, slip stability, and permeability of quartz and talc mixtures in each of two configurations: uniform mixtures and layered mixtures. We estimate the local permeability from the evolution of local porosity measured in seven spherical control volumes arranged along the shear localization zone. The relationship between the evolution of porosity and permeability is given by Samuelson et al. (2011)

$$\frac{k}{k_0} \cong (1 + \Delta\phi)^3 \tag{18}$$

where k/k_0 is the relative ratio of current to initial permeability and $\Delta\phi$ is the change in average local porosity.

The uniform mixtures comprise uniformly distributed quartz and talc analog particles representing mass fractions from 0:100% to 100:0% quartz:talc. The layered mixtures consist of a thin layer of talc analog sandwiched within a quartz matrix with a variable thickness of 1 particle, 3 particles, 5 particles, 8 particles, and 10 particles across the talc layer at the initiation of each test. The detailed list of simulations is presented in Table 2.

4. Results

Direct shear simulations with a prescribed velocity schedule are conducted for mixtures of quartz and talc analogs under controlled normal stress and prescribed shear velocities. Both uniform and layered mixtures are used to define the evolution of shear strength, stability parameters, and permeability.

4.1. Evolution of Shear Strength

Simulations of direct shear tests are conducted on uniform and layered mixtures of quartz and talc analogs. Since the normal stress in all simulations is identical (10 MPa), we use the shear strength evolution to represent the ensemble friction coefficient of the mixture. The full friction evolution of the uniform mixtures and layered mixtures is shown in Figure 3.
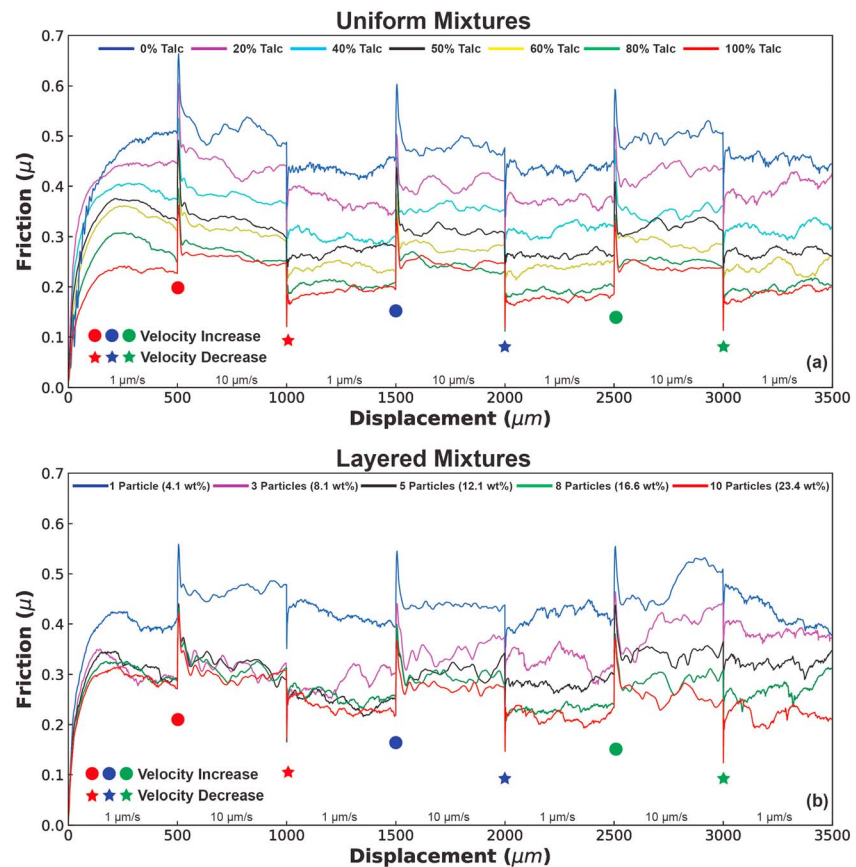
Figure 3. (a) Friction evolution of representative uniform talc-quartz mixtures, that is, 0%, 20%, 40%, 50%, 60%, 80%, and 100% talc-quartz mixtures. (b) Friction evolution of layered mixtures, that is, 1 particle (4.1 wt %), 3 particles (8.1 wt %), 5 particles (12.1 wt %), 8 particles (16.6 wt %), and 10 particles (23.4 wt %) talc.

The friction coefficient of uniform mixtures after a shear displacement of 500 μm is summarized in Figure 4. It is clearly observed that an increase in talc content results in a reduction in shear strength. With 50% talc, the friction coefficient of the mixture is reduced from ~0.52 to ~0.34, from that of 100% quartz. The weakening continues with >50% talc.

The frictional evolution of a layered mixture is also shown in Figure 4. The friction coefficient decreases with an increase in talc layer thickness. Specifically, friction decreases from ~0.52 to <0.3 with ~8 wt % of talc (relative layer thickness of three particles) present in the mixture. This trend is consistent with previous laboratory observations (Niemeijer et al., 2010) and 2D simulation results using DEM (Wang et al., 2017).

4.2. Evolution of Slip Stability

Previous laboratory observations suggest that talc can affect the slip stability of faults comprising a strong tectosilicate matrix. Specifically, the presence of talc can increase the value of the stability parameter $(a - b)$ with increasing weight percentage. Gouge mixtures of quartz and talc show a transition from velocity weakening to velocity strengthening at 25–50 wt % talc; calcite and talc mixtures show mainly velocity strengthening behavior (Giorgetti et al., 2015; Moore & Lockner, 2011). This strong influence of talc on behavior has been simulated using 2D DEM modeling (Wang et al., 2017). In this study, we conduct velocity stepping simulations on quartz and talc mixtures using a modified slip-weakening constitutive law.

Zooming into friction evolution at each velocity step enables the analysis of stability parameters, that is, $(a - b)$ values. The friction evolution of each velocity step is best fitted by a rate and state friction law using an iterative Levenberg-Marquardt (L-M) algorithm (Press et al., 1987). In the fitting process, a set of initial guesses for a and b values is made. The L-M algorithm then searches from a range of 0.001 to 1000 times
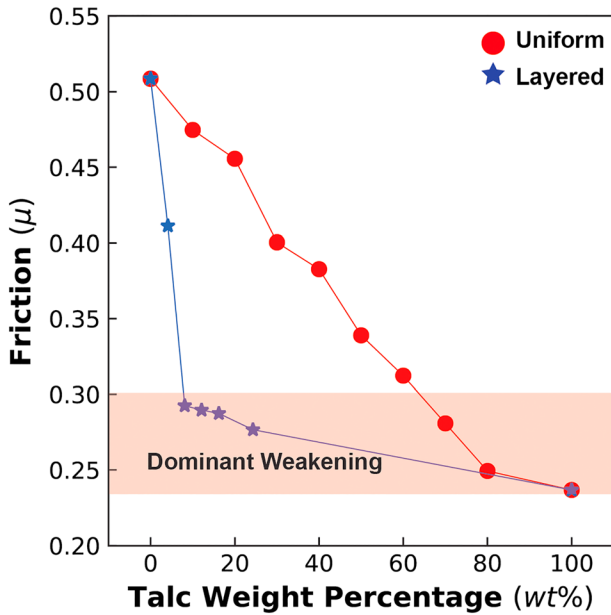
Figure 4. Friction coefficient after 500 μm of shear displacement. Significant weakening in the uniform mixture occurs at >50 wt % talc, while ~8 wt % of talc can induce a similar weakening effect in the layered mixtures.

the initial estimations. The algorithm fits the evolution curve by solving the rate and state friction law using a fourth-order Runge-Kutta algorithm (Press et al., 1987). The algorithm converges at conditions where both the difference between the previous and current trial parameter or Chi square of the fitted data is sufficiently small. Figures 5a and 5b show the fitted $(a − b)$ values analyzed from uniform mixtures and layered mixtures, respectively.

Figures 5a and 5b shows a summarized plot of $(a − b)$ values of corresponding velocity steps marked in Figure 3, as well as trendlines of $(a − b)$ values from the same velocity steps from different simulations. The $(a − b)$ values are mostly positive in both uniform and layered mixtures. The positive slopes of $(a − b)$ trendlines suggest that, in uniform mixtures, an increase in talc content can increase the $(a − b)$ value, with the exception of the first velocity-increase step (negative slope). The exception may be explained by the bulk gouge not reaching steady state after 500 μm of initial shear displacement. The $(a − b)$ values do not show apparent trends with increasing thickness of talc layer, suggested by scattered data and trendline slopes.

4.3. Evolution of Layer Thickness, Coordination Number, and Local Permeability

The permeability of reactivated faults will evolve as the fault slips. The permeability of fault gouge is related to the evolution of layer thickness and porosity (Samuelson et al., 2009). We represent the overall evolution of the layer thickness by monitoring the dilation of gouge during the experiment. Local permeability evolution is also determined from local changes in porosity recorded during shear. The original and detrended sample layer thicknesses of 10% and 90% uniform talc-quartz mixtures are shown in Figures 6a and 6b, respectively. Geometric thinning is detrended by removing the linear decreasing trend of the layer thickness evolution. Both cases show dilation during fast-loading velocity steps and compaction during slow-loading velocity steps. Specifically, the 90% talc-quartz mixture shows strong initial compaction at velocity decrease steps, that is, when velocity drops from 10 to 1 μm/s, but the compaction continues in a reduced rate until the next velocity step. However, the 10% talc-quartz mixture does not feature such an apparent two-step compaction during the 10- to 1-μm/s velocity step. The local permeability of the 10% and 90% talc quartz mixture is shown in Figure 6c. The 10% talc-quartz mixture shows an initial increase in local permeability, followed by a sharp decrease at ~2,000 μm of shear displacement, and continues to slowly level off afterward. The 90% talc-quartz mixture shows a sharp decrease in local permeability at ~1,000 μm of shear displacement and
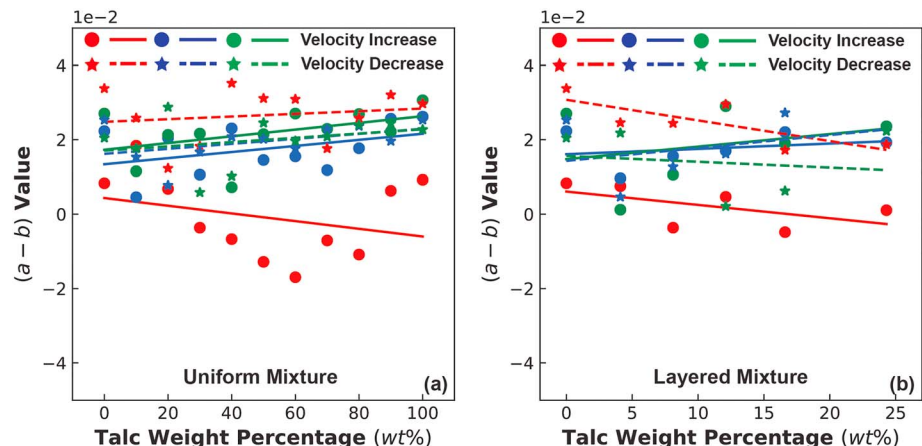

Figure 5. (a) $(a − b)$ of uniform mixture plotted against talc weight percentage; (b) $(a − b)$ of layered mixture plotted against talc weight percentage. The markers correspond to the velocity steps shown in Figure 3.
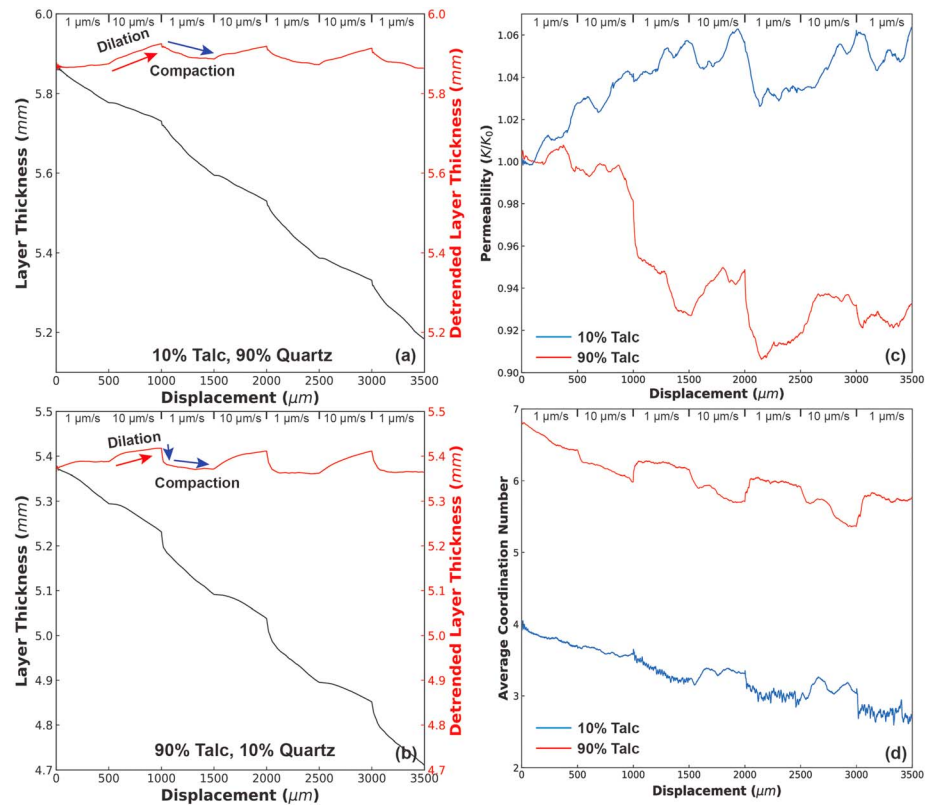
Figure 6. Original/detrended evolution of sample layer thickness with shear displacement for (a) 10% talc-quartz mixture and (b) 90% talc-quartz mixture. (c) Local normalized permeability evolution of 10% and 90% talc-quartz mixtures estimated from local porosity evolution. (d) Evolution of average coordination number of 10% and 90% talc-quartz mixtures.

stabilizes after ~2,000 μm. In both cases, the local permeability decreases after a velocity drop but recovers slightly before the next change in velocity, suggesting a maturation of a localization zone. However, this behavior is not apparent before ~1,000 and ~2,000 μm of shear offset for 90% and 10% talc-quartz mixtures, respectively, suggesting that higher content of talc may accelerate the development of a shear localization zone.

The average coordination numbers (the average number of active contacts around each particle) of the 10% and 90% talc-quartz mixtures are shown in Figure 6d. Both cases show an overall decrease in coordination number with shear offset, which is consistent with the observation of long-term dilation. The 10% talc-quartz mixture shows significantly lower average coordination number than the 90% talc-quartz mixture, indicating a less dense packing. In the case of the 90% talc-quartz mixture, the average coordination number increases with a velocity decrease, with the converse behavior observed for the 10% talc-quartz mixture. These observed behaviors can be viewed as the additive effect of compaction, dilation, and self-rearrangement. Quartz exhibits a higher shear strength, contact rolling resistance and is incapable of rapid rearrangement, suggested by the negligible compaction after a velocity drop (Figure 6a). Talc exhibits significantly smaller contact friction and thus may self-rearrange rapidly—reflected in the slight dilation (decrease in coordination number) promoted by a velocity increase and rapid compaction (increase in coordination number) caused by a velocity decrease. Given the nonperiodic model configuration, the extruded particles at the two ends feature less dense packing than the effective shear zone in the quartz-rich mixtures; however, they feature similar packing to the shear zone in the talc-rich mixtures. Higher shear velocity may promote self-rearrangement of the quartz-rich gouge in the nonperiodic system, thus increasing coordination number during velocity increases. This observed rate of self-rearrangement is also suspected to be related to normal stress, that is, higher normal stress may reduce the effect of self-rearrangement thus neutralizing the difference of velocity-dependent compaction and dilation behavior between talc-rich and quartz-rich gouge.

5. Discussion

5.1. Shear Localization and Permeability Evolution

Uniform mixtures of quartz and talc show a linear trend of weakening, while layered mixtures show a non-linear (exponential) trend in our simulation results. In laboratory experiments, dominant weakening of talc is commonly observed. Our observation of uniform mixtures matches previous laboratory observations (Moore & Lockner, 2011) but contradicts other laboratory observations of dominant weakening at ~25% talc in uniform mixtures (Giorgetti et al., 2015), and 2D simulation results using a similar DEM model (Wang et al., 2017). However, the dominant weakening trend of layered mixtures in our simulation matches laboratory observations very well (Niemeijer et al., 2010). In a granular gouge system, the transient shear strength is determined by ensemble strength of force chains formed during shear. Weak patches can reduce the number of effective strong force chains or hinder strong force chains in forming. Talc particles feature much lower surface friction and elastic contact stiffness than quartz particles, thus acting as a weak patch in the quartz matrix by connecting quartz particles as shown in Figure 7a. The weakening behavior of quartz-talc mixtures is believed to be caused by the connection of weak talc patches in the uniform mixtures and shear localization in the layered mixtures. Introducing more talc by weight increases the number of weak patches as well as their affected areas. Weak patches are often preferentially self-relocated along the shear zone after a certain amount of shearing. The weakening effect can be largely enhanced if the weak particles (patches) are preimposed as a through-going layer in the gouge, forming a connected weak zone as shown in Figure 7b. The weak zone prevents the formation of stronger force chains and significantly reduces the ensemble shear strength.

Figures 7c and 7d show the filtered contact friction map of the uniform mixture and layered mixture at a shear displacement of 3,000 μm, at the end of a velocity increase. Weak contacts with friction in the range 0.106 to 0.100 (according to the slip-weakening law introduced in section 2.1) are plotted, representing the evolved contacts in the assembly where the majority of shear displacement is accommodated. Strong contacts with friction coefficient outside the range (0.1 to 0.106) are not shown (filtered). It can be clearly observed that these contacts are mainly distributed in the Riedel-shear direction in the uniform mixtures.

In layered mixtures, the weak talc patches are initially preconnected and are preimposed as a through-going layer, resulting in strong weakening and localization. In this configuration, the talc layer transects the gouge and prevents these mechanically isolated quartz particles from forming strong force chains, creating a barrier effect. However, when the talc layer is relatively thin, some quartz particles penetrate the talc layer and form continuous force chains across the horizontal transect and between shear platens. Increasing talc layer thickness enhances the barrier effect, obviating the penetration of quartz across the talc. Therefore, the observation of a strong weakening effect with an increase in the thickness of the talc layer is rational. The force chains are truncated mostly at the boundary of the talc layer. Figure 8 shows the assembly at a shear displacement of 3,500 μm with talc weight percentages of 4.1%, 8.1%, 12.1%, 16.6%, and 24.3% (these weight percentages correspond to the relative talc layer thickness of 1 particle, 3 particles, 5 particles, 8 particles, and 10 particles, respectively). Penetration of quartz through the talc layer is clearly decreased as the talc layer thickness is increased (Figures 8a–8e). A major increase in shear localization is observed between 4.1% talc and 8.1% talc, suggested by the strong weakening effect (large drop in friction shown in Figure 4). Minor differences are observed with even greater talc layer thicknesses, indicating a dominant effect.

The volume and interconnectivity of pore volume are linked directly to the permeability of the porous media. Porosity is often measured as a proxy for permeability although requires scaling against a necessary length dimension. In this study, the permeability of the gouge is estimated from porosity measured in seven (spherical) sampling windows, spaced along the shear zone, overlapping with the localization zone. The evolution of porosity during dynamic shear in the localization zone accounts for the permeability evolution. We have shown a distinct difference in permeability evolution between the 90% talc (talc-rich) gouge and 10% talc (quartz-rich) gouge mixtures (Figure 6c). Specifically, permeability decreases with talc-rich gouge while increases with quartz-rich gouge. This distinct behavior is plausibly caused by different elastic properties and frictional resistance of quartz and talc contacts. Contacts between quartz grains feature much higher contact stiffness and friction than talc, indicating a large potential for shear dilation rather than shear compaction during shear. Contacts between talc grains or contacts between talc and quartz grains are weakened
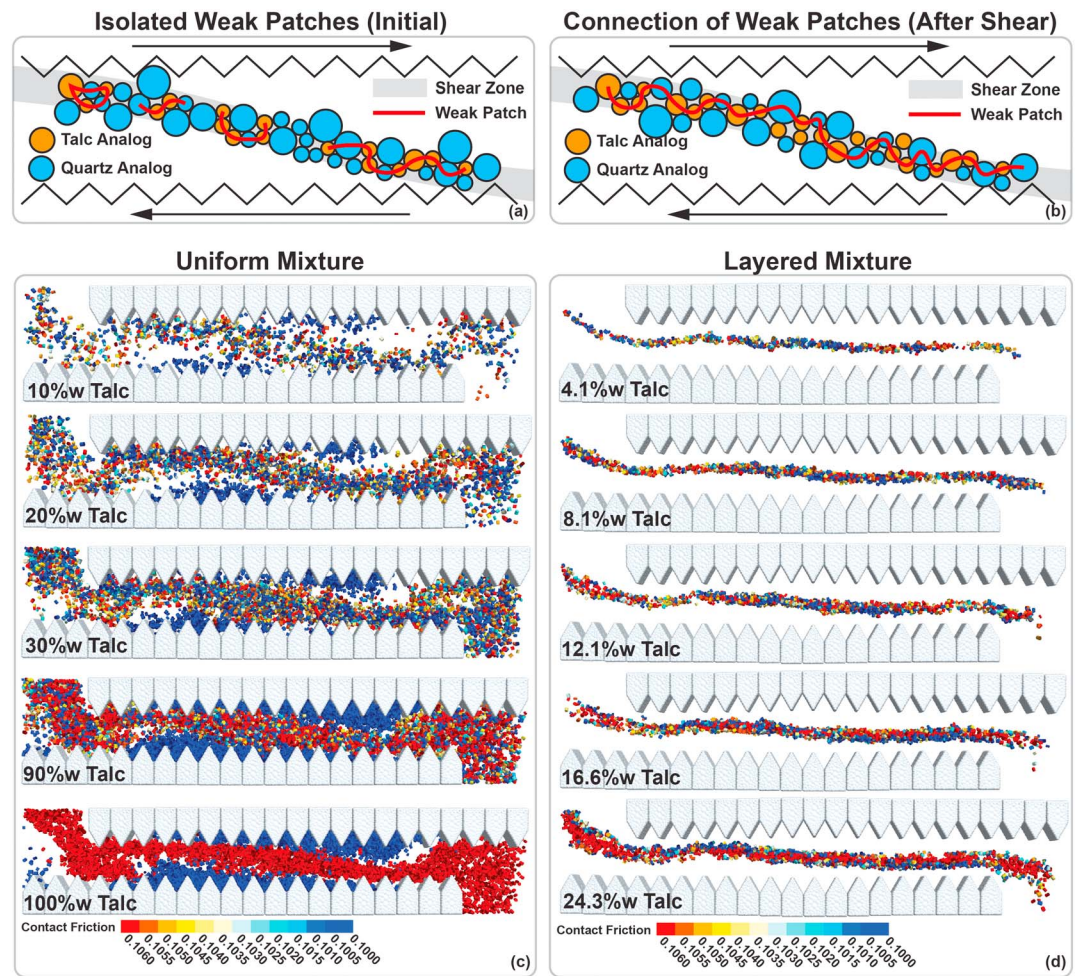
Figure 7. (a) Schematic of weak patches formed by talc. (b) Schematic of weak patches preferentially self-rearranged into a shear zone after a given shear displacement. (c) Evolved weak contacts in a uniform mixture oriented along the R-shear direction. (d) Evolved weak contacts in layered mixture only appear in the talc layer, indicating strong localization.

by talc, in terms of both elastic properties and friction. Therefore, these contacts are less prone to shear dilation, exhibiting shear compaction and thus destroying permeability. Notably, once the gouge accumulates a certain amount of shear displacement (~2,000 μm in this study), the overall local porosity stabilizes, implying an overall steady state permeability and a maturation of shear localization. In nature, talc grains are platy, deformable, and featuring a tendency toward self-organization to align with the shear localization direction. These features increase the number of weakened contacts, therefore enhancing the weakening effect and shear compactive nature of talc.

5.2. Modeling of Stability Parameters

The DEM modeling of the enhancement of shear stability (increase in $[a - b]$ values) with an increasing proportion of talc matches well with previous studies. However, the stability parameters (a and b) applied to the analog minerals in this study are approximately one order-of-magnitude larger than laboratory measured values and are always positive. Previous laboratory studies suggest that phyllosilicates feature negative b values, which is presumably due to the platy particle shape (Giorgetti et al., 2015). In the DEM model, spherical particles are implemented to conduct the simulations. The spherical grain shape could result in greater geometric dilation and produce increased numerical noise as shear strength evolves. This numerical noise would mask the evolution in instability and hinder the direct assignment of lab-measured stability parameters. Three-dimensional DEM simulations are often computationally expensive. To counter this drawback, a density scaling factor of 10^{12} is implemented to reduce the
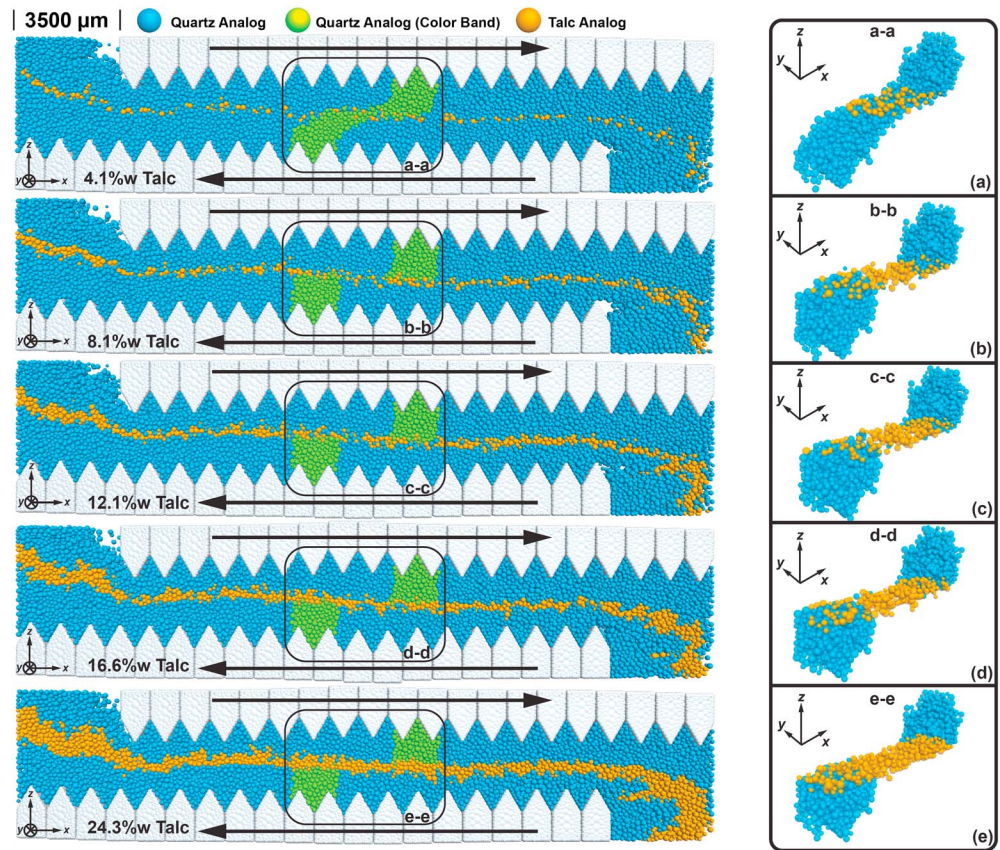
Figure 8. Localization of shear deformation in a layered mixture. The green band shows the deformation pattern of the gouge for different talc layer thicknesses. Penetration of quartz through the talc layer is reduced by an increased talc layer thickness. A major difference in shear localization is observed between 4.1% talc and 8.1% talc, as a strong weakening effect is observed; however, only minor differences are observed for greater talc layer thicknesses.

computational time to a feasible range (around 24 hr on current hardware). Reducing the density scaling factor by 2 orders-of-magnitude results in a 1 order-of-magnitude increase in the computational time. Density scaling may induce additional inertial effect on velocity change events that can affect the magnitude of $(a - b)$ values, that is, a large density scaling factor can increase the value of a. We use density scaling and exaggerated a and b values to, first, unmask the stability behavior from the numerical noise. The scaling up of stability parameters a and b improves the resolution of the instantaneous response to velocity change during dynamic shear with velocity steps. Second, we focus on defining the transition in slip stability behavior, that is, exploring the evolution trends of $(a - b)$. The large magnitude of the selected stability parameters and density scaling is unlikely to influence the evolution trend of stability parameters for the various gouge compositions—and regardless, comparative results will return valid trends. Third, the precise reproduction of rate and state response using DEM remains a major challenge and is beyond the principal foci of this study. Nevertheless, this study provides useful insights in approaching the problem via appropriate simplifications.

5.3. Effect of Grain Size and Grain Shape

A rolling resistance mechanism is implemented at particle contacts to mimic grain angularity and interlocking. Previous simulation studies have considered grain angularity, anisotropy, local rate and state friction, and grain deformation (Abe & Mair, 2009; Guo & Morgan, 2004; Kim et al., 2016; Mair et al., 2002). However, these physical features and mechanisms are never combined into a single numerical model, as doing so makes the model overly complicated and computationally expensive. In this study, we specifically explore the evolution of shear strength, slip stability, and permeability of quartz and talc analog mixtures. Nonetheless, grain size and grain shape no doubt play a key role in determining the resolution of the
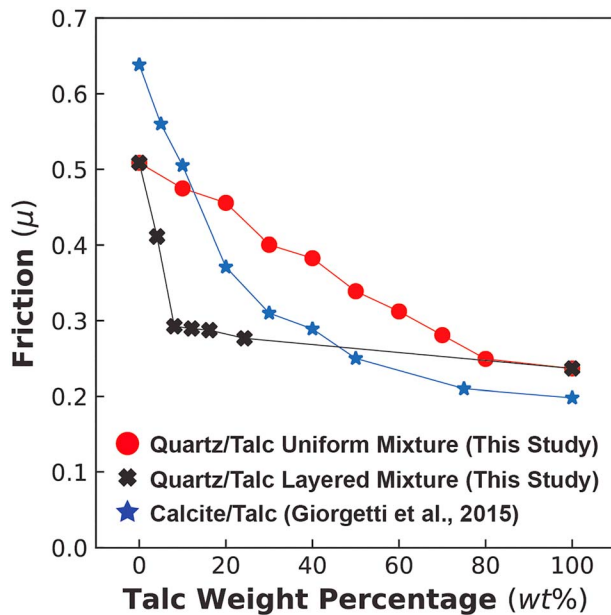
Figure 9. Comparison of weakening effect of talc explored in this study relative to previous laboratory results using calcite-talc mixtures (Giorgetti et al., 2015). Data are replotted from original paper.

simulation and the transitional behavior of the mixture. Reducing particle size can improve the resolution of shear strength evolution (Wang et al., 2017); however, a smaller grain size necessarily increases the number of particles in the assembly—this is especially true in 3D space—resulting in increased computational cost. We manage to achieve a balance between the choice of grain size, computational cost, and resolution of the simulation.

The drawback of spherical particles, in allowing unfettered rolling, is well understood but can be countered by adding rolling resistance to the particle contact. The aspect of quartz particles generally ranges from near spherical to angular, and that of talc is platy. These are the key microscopic features that dictate distinct frictional properties. Platy talc particles would be anticipated to form increased contacts with quartz particles, with this, coupled with its high deformability, providing the potential to create large weakening areas. The microscopic weakening mechanism for talc mixtures may be related to the deformation and self-reorientation of the platy particles, as well as strong mineral particles tend to slide along the platy interfaces of talc particles in an angular grain matrix, forming localized weak patches. These weak patches are self-organizing and localized in the shear zone to further weaken the bulk gouge during shear (Giorgetti et al., 2015). This weakening mechanism applies to both uniform and layered mixture. However, a threshold shear strain is required in uniform mixtures for talc deformations to localize, while this localization has already been preimposed in layered mixtures. The numerical simulations in this study are compared to previous laboratory data in Figure 9. The numerical results of uniform mixtures in this study differ by ~10 to ~20% in terms of the transition from dominantly frictionally strong to dominantly frictionally weak, resulting from the spherically shaped grains in the model. However, the weakening effect of a preimposed localization (layered mixtures) shown by our simulation is mechanistically similar to that of laboratory results, due to the fact that platy talc particles promote localization in uniform mixtures by forming through-going talc-rich layers. Full implementation of platy grains with appropriate high deformability could be achieved in a future study. Nonetheless, we argue that our simulation results show an overall creditable match with previous laboratory and simulation results, especially for the layered mixture configuration (Niemeijer et al., 2010), which is most likely to appear in nature.

5.4. Comparison of 3D and 2D Response

The effect of problem dimensionality on the shear strength of gouge has been studied both in the laboratory and in numerical simulations. In laboratory studies, metal rods were used to represent the 2D configuration (Knuth & Marone, 2007) and behavior was compared to experiments using glass beads (3D). Two-dimensional materials have a high potential for dilation and compaction, creating large fluctuations in shear strength during shear evolution. Additionally, due to the strong tendency for the rolling of rods, the friction coefficient in the 2D configuration is reduced (maximum of ~0.35). Numerical studies of 2D direct shear on gouge (Morgan & Boettcher, 1999; Wang et al., 2017) indicate similar friction evolution and fluctuation to laboratory results on metal rods. Realistic magnitudes of friction can only be reproduced by fully restraining the rotation of particles. We compare the resolution of friction evolution from previous 2D simulation with particle rotation disabled (Wang et al., 2017) and 3D simulation in this study. Figures 10a and 10b show the simulated evolution of friction of 100% analog quartz in both 2D and 3D configurations where model parameters are consistent. A significant reduction in fluctuations is observed in the 3D evolution. The direct effect and evolution effect of rate and state friction are independently apparent in 3D but are almost masked in 2D.

In terms of reducing fluctuations in shear strength evolution, the additional dimension and related extra displacement degree of freedom in 3D reduce the strong dilation effect apparent in 2D. For example, particles that need to override other particles to rearrange in 2D are able to move both obliquely and sideways in 3D.
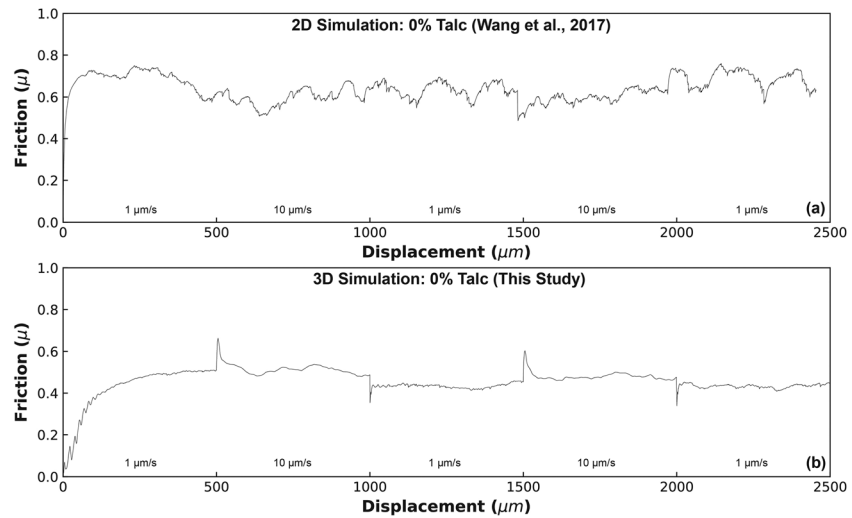
Figure 10. Comparison of 2D and 3D simulations: (a) 2D friction evolution of 0% talc under dynamic shear (Wang et al., 2017) and (b) 3D friction evolution of 0% talc under dynamic shear (this study).

This 3D rearrangement in our numerical model better accommodates the natural rearrangement of gouge grains during shear.

Three-dimensional numerical simulations also show an improved representation of the direct and evolution effects described by rate and state friction. This is plausibly due to the increase in the number of contacts in the 3D configuration. The average coordination number is nearly double that in 2D. This indicates that more contacts are evolving during a velocity step, resulting in a crispier resolution.

6. Conclusions

In this study, we explore the shear strength, slip stability, and permeability of analog quartz and talc mixtures via 3D distinct element modeling. Specifically, configurations of both uniform and layered mixtures with various talc:quartz weight proportions are examined. We perform numerical direct shear tests with velocity stepping on the sample mixtures and capture the evolution of shear strength, slip stability, and permeability. We conclude the following based on the observed results.

1. Simulations show strong weakening effects in uniform mixtures of talc; 50% of talc in uniform mixtures can induce strong weakening effect in shear strength. A dominant weakening effect is observed for layered talc, that is, a mixture with a thickness of three particles of talc can induce an ~50% reduction in shear strength.
2. Increased talc content can enhance the stability of uniform mixtures by increasing $(a - b)$ values; however, no apparent relationship between talc layer thickness and the stability behavior in layered mixtures is observed.
3. In uniform mixtures, permeability increases with increased quartz content before the maturation of shear localization, showing no apparent response with velocity steps. Permeability evolves to a steady state after the maturation of shear localization and is enhanced with velocity upsteps and depressed with downsteps.
4. Frictionally weak minerals (talc) self-organize and self-localize in imbricate structures that form weakened patches that grow and interconnect to form a shear zone, enhance shear localization and thus dominate the frictional and rheological responses of faults. This effect is enhanced by preexisting layering and potentially by the natural platy form of the mineral.

The results fit previous laboratory observations while some slight mismatches are also noticed. These inaccuracies can be related to the idealized particle shape and size distribution, simplified to spherical in these mixtures. Future research of full implementation of realistic particle shape and deformable grains needs to be achieved to better simulate the behavior of faults during shear. Nonetheless, our work shows an alternative way of exploring the rheological properties of faults during dynamic shear.

References

Abe, S., Dieterich, J. H., Mora, P., & Place, D. (2002). Simulation of the influence of rate- and state-dependent friction on the macroscopic behavior of complex fault zones with the lattice solid model. *Pure and Applied Geophysics*, *159*(9), 1967–1983. https://doi.org/10.1007/s00024-002-8718-7

Abe, S., & Mair, K. (2009). Effects of gouge fragment shape on fault friction: New 3D modelling results. *Geophysical Research Letters*, *36*, L23302. https://doi.org/10.1029/2009GL040684

Abe, S., van Gent, H., & Urai, J. L. (2011). DEM simulation of normal faults in cohesive materials. *Tectonophysics*, *512*(1–4), 12–21. https://doi.org/10.1016/j.tecto.2011.09.008

Ai, J., Chen, J. F., Rotter, J. M., & Ooi, J. Y. (2011). Assessment of rolling resistance models in discrete element simulations. *Powder Technology*, *206*(3), 269–282. https://doi.org/10.1016/j.powtec.2010.09.030

Anthony, J. L., & Marone, C. (2005). Influence of particle characteristics on granular friction. *Journal of Geophysical Research*, *110*, B08409, 1–14. https://doi.org/10.1029/2004JB003399

Collettini, C., & Holdsworth, R. E. (2004). Fault zone weakening and character of slip along low-angle normal faults: Insights from the Zuccale fault, Elba, Italy. *Journal of the Geological Society*, *161*(6), 1039–1051. https://doi.org/10.1144/0016-764903-179

Cundall, P. A., & Strack, O. D. L. (1979). A discrete numerical model for granular assemblies. *Géotechnique*, *29*(1), 47–65. https://doi.org/10.1680/geot.1979.29.1.47

Dieterich, J. H. (1979). Modeling of rock friction 1. Experimental results and constitutive equations. *Journal of Geophysical Research*, *84*(B5), 2161–2168. https://doi.org/10.1029/JB084iB05p02161

Dieterich, J. H. (1992). Earthquake nucleation on faults with rate-and state-dependent strength. *Tectonophysics*, *211*(1–4), 115–134. https://doi.org/10.1016/0040-1951(92)90055-B

D'Orazio, M., Boschi, C., & Brunelli, D. (2004). Talc-rich hydrothermal rocks from the St. Paul and Conrad fracture zones in the Atlantic Ocean. *European Journal of Mineralogy*, *16*(1), 73–83. https://doi.org/10.1127/0935-1221/2004/0016-0073

Escartín, J., Andreani, M., Hirth, G., & Evans, B. (2008). Relationships between the microstructural evolution and the rheology of talc at elevated pressures and temperatures. *Earth and Planetary Science Letters*, *268*(3–4), 463–475. https://doi.org/10.1016/j.epsl.2008.02.004

Fang, Y., Elsworth, D., Wang, C., & Jia, Y. (2018). Mineralogical controls on frictional strength, stability, and shear permeability evolution of fractures. *Journal of Geophysical Research: Solid Earth*, *123*, 3549–3563. https://doi.org/10.1029/2017JB015338

Faulkner, D. R., Jackson, C. A. L., Lunn, R. J., Schlische, R. W., Shipton, Z. K., Wibberley, C. A. J., & Withjack, M. O. (2010). A review of recent developments concerning the structure, mechanics and fluid flow properties of fault zones. *Journal of Structural Geology*, *32*(11), 1557–1575. https://doi.org/10.1016/j.jsg.2010.06.009

Faulkner, D. R., Lewis, A. C., & Rutter, E. H. (2003). On the internal structure and mechanics of large strike-slip fault zones: Field observations of the Carboneras fault in southeastern Spain. *Tectonophysics*, *367*(3–4), 235–251. https://doi.org/10.1016/S0040-1951(03)00134-3

Ferdowsi, B., Griffa, M., Guyer, R. A., Johnson, P. A., Marone, C., & Carmeliet, J. (2014). Three-dimensional discrete element modeling of triggered slip in sheared granular media. *Physical Review E - Statistical, Nonlinear, and Soft Matter Physics*, *89*, 1–12. https://doi.org/10.1103/PhysRevE.89.042204

Gao, K., Euser, B. J., Rougier, E., Guyer, R. A., Lei, Z., Knight, E. E., et al. (2018). Modeling of stick-slip behavior in sheared granular fault gouge using the combined finite-discrete element method. *Journal of Geophysical Research: Solid Earth*, *123*, 5774–5792. https://doi.org/10.1029/2018JB015668

Giorgetti, C., Carpenter, B. M., & Collettini, C. (2015). Frictional behavior of talc-calcite mixtures. *Journal of Geophysical Research: Solid Earth*, *120*, 6614–6633. https://doi.org/10.1002/2015JB011970

Grasemann, B., & Tschegg, C. (2012). Localization of deformation triggered by chemo-mechanical feedback processes. *Bulletin of the Geological Society of America*, *124*(5–6), 737–745. https://doi.org/10.1130/B30504.1

Guan, C.-Y., Qi, J.-F., Qiu, N.-S., Zhao, G.-C., Yang, Q., Bai, X.-D., & Wang, C. (2012). Macroscopic Young's elastic Modulus model of particle packing rock layers. *Open Journal of Geology*, *02*(03), 198–202. https://doi.org/10.4236/ojg.2012.23020

Guo, Y., & Morgan, J. K. (2004). Influence of normal stress and grain shape on granular friction: Results of discrete element simulations. *Journal of Geophysical Research*, *109*, B12305. https://doi.org/10.1029/2004JB003044

Hazzard, J. F., & Mair, K. (2003). The importance of the third dimension in granular shear. *Geophysical Research Letters*, *30*(13), 1708. https://doi.org/10.1029/2003GL017534

Ikari, M. J., Marone, C., & Saffer, D. M. (2011). On the relation between fault strength and frictional stability. *Geology*, *39*(1), 83–86. https://doi.org/10.1130/G31416.1

Iwashita, K., & Oda, M. (1998). Rolling resistance at contacts in simulation of shear band development by DEM. *Journal of Engineering Mechanics*, *124*(3), 285–292. https://doi.org/10.1061/(ASCE)0733-9399(1998)124:3(285)

Jiang, M., Shen, Z., & Wang, J. (2015). A novel three-dimensional contact model for granulates incorporating rolling and twisting resistances. *Computers and Geotechnics*, *65*, 147–163. https://doi.org/10.1016/j.compgeo.2014.12.011

Kim, K. Y., Suh, H. S., Yun, T. S., Moon, S.-W., & Seo, Y.-S. (2016). Effect of particle shape on the shear strength of fault gouge. *Geosciences Journal*, *20*(3), 351–359. https://doi.org/10.1007/s12303-015-0051-0

Knuth, M., & Marone, C. (2007). Friction of sheared granular layers: Role of particle dimensionality, surface roughness, and material properties. *Geochemistry, Geophysics, Geosystems*, *8*, Q03012. https://doi.org/10.1029/2006GC001327

Mair, K., Frye, K. M., & Marone, C. (2002). Influence of grain characteristics on the friction of granular shear zones. *Journal of Geophysical Research*, *107*, 2219. https://doi.org/10.1029/2001JB000516

Mair, K., & Marone, C. (1999). Friction of simulated fault gouge for a wide range of velocities and normal stresses. *Journal of Geophysical Research*, *104*(B12), 28,899–28,914. https://doi.org/10.1029/1999JB900279

Marone, C. (1998). Laboratory-derived friction Laws and Their application to seismic faulting. *Annual Review of Earth and Planetary Sciences*, *26*(1), 643–696. https://doi.org/10.1146/annurev.earth.26.1.643

Marone, C., Raleigh, C. B., & Scholz, C. H. (1990). Frictional behavior and constitutive modeling of simulated fault gouge. *Journal of Geophysical Research*, *95*(B5), 7007–7025. https://doi.org/10.1029/JB095iB05p07007

Moore, D. E., & Lockner, D. A. (2011). Frictional strengths of talc-serpentine and talc-quartz mixtures. *Journal of Geophysical Research*, *116*, B01403. https://doi.org/10.1029/2010JB007881

Moore, D. E., & Rymer, M. J. (2007). Talc-bearing serpentinite and the creeping section of the San Andreas fault. *Nature*, *448*(7155), 795–797. https://doi.org/10.1038/nature06064

Morgan, J. K. (1999). Numerical simulations of granular shear zones using the distinct element method: 2. Effects of particle size distribution and interparticle friction on mechanical behavior. *Journal of Geophysical Research*, *104*(B2), 2721. https://doi.org/10.1029/1998JB900055–2732

Morgan, J. K. (2004). Particle dynamics simulations of rate- and state-dependent frictional sliding of granular fault gouge. *Pure and Applied Geophysics*, *161*(9–10), 1877–1891. https://doi.org/10.1007/s00024-004-2537-y

Morgan, J. K., & Boettcher, M. S. (1999). Numerical simulations of granular shear zones using the distinct element method: 1. Shear zone kinematics and the micromechanics of localization. Journal of Geophysical Research *104*(B2), 2703–2719. https://doi.org/10.1029/1998JB900056

Niemeijer, A. R., Marone, C., & Elsworth, D. (2010). Fabric induced weakness of tectonic faults. *Geophysical Research Letters*, *37*, L03304. https://doi.org/10.1029/2009GL041689

Peacock, S. M. (1987). Inverted metamorphic gradients of New England. *Journal of Geophysical Research*, *92*(B12), 12,763–12,781. https://doi.org/10.1029/JB092iB12p12763

Press, W., Flannery, B., Teukolsky, S., & Vetterling, W. (1987). Numerical recipes: The art of scientific computing. *Technometrics*, *29*(4), 501. https://doi.org/10.2307/1269484

Ruina, A. (1983). Slip instability and state variable friction laws. *Journal of Geophysical Research*, *88*(B12), 10,359–10,370. https://doi.org/10.1029/JB088iB12p10359

Samuelson, J., Elsworth, D., & Marone, C. (2009). Shear-induced dilatancy of fluid-saturated faults: Experiment and theory. *Journal of Geophysical Research*, *114*, B12404. https://doi.org/10.1029/2008JB006273

Samuelson, J., Elsworth, D., & Marone, C. (2011). Influence of dilatancy on the frictional constitutive behavior of a saturated fault zone under a variety of drainage conditions. *Journal of Geophysical Research*, *116*, B10406. https://doi.org/10.1029/2011JB008556

Scholz, C. H. (1998). Earthquakes and friction laws. *Nature*, *391*(6662), 37–42. https://doi.org/10.1038/34097

Sun, Z., Espinoza, D. N., & Balhoff, M. T. (2016). Discrete element modeling of indentation tests to investigate mechanisms of CO2-related chemomechanical rock alteration. *Journal of Geophysical Research: Solid Earth*, *121*, 7867–7881. https://doi.org/10.1002/2016JB013554

Taylor, B., & Huchon, P. (2002). Active continental extension in the western Woodlark basin: A synthesis of Leg 180 results. *Proceedings of the Ocean Drilling Program, 180 Scientific Results*, *180*(July 2001). https://doi.org/10.2973/odp.proc.sr.180.150.2002

van den Ende, M. P. A., Marketos, G., Niemeijer, A. R., & Spiers, C. J. (2018). Investigating compaction by intergranular pressure solution using the discrete element method. *Journal of Geophysical Research: Solid Earth*, *123*, 107–124. https://doi.org/10.1002/2017JB014440

Viti, C., & Collettini, C. (2009). Growth and deformation mechanisms of talc along a natural fault: A micro/nanostructural investigation. *Contributions to Mineralogy and Petrology*, *158*(4), 529–542. https://doi.org/10.1007/s00410-009-0395-4

Vrolijk, P., & Van Der Pluijm, B. A. (1999). Clay gouge. *Journal of Structural Geology*, *21*(8–9), 1039–1048. https://doi.org/10.1016/S0191-8141(99)00103-0

Wang, C., Elsworth, D., & Fang, Y. (2017). Influence of weakening minerals on ensemble strength and slip stability of faults. *Journal of Geophysical Research: Solid Earth*, *122*, 7090–7110. https://doi.org/10.1002/2016JB013687

Wensrich, C. M., & Katterfeld, A. (2012). Rolling friction as a technique for modelling particle shape in DEM. *Powder Technology*, *217*, 409–417. https://doi.org/10.1016/j.powtec.2011.10.057

Wintsch, R. P., Christoffersen, R., & Kronenberg, A. K. (1995). Fluid-rock reaction weakening of fault zones. *Journal of Geophysical Research*, *100*(B7), 13,021–13,032. https://doi.org/10.1029/94JB02622